

# Power conversion efficiency exceeding the Shockley–Queisser limit in a ferroelectric insulator

Jonathan E. Spanier<sup>1,2,3\*†</sup>, Vladimir M. Fridkin<sup>2,4†</sup>, Andrew M. Rappe<sup>5</sup>, Andrew R. Akbashev<sup>1</sup>, Alessia Polemi<sup>1</sup>, Yubo Qi<sup>5</sup>, Zongquan Gu<sup>3</sup>, Steve M. Young<sup>6</sup>, Christopher J. Hawley<sup>1</sup>, Dominic Imbrenda<sup>3</sup>, Geoffrey Xiao<sup>1</sup>, Andrew L. Bennett-Jackson<sup>1</sup> and Craig L. Johnson<sup>1</sup>

**Ferroelectric absorbers, which promote carrier separation and exhibit above-gap photovoltages, are attractive candidates for constructing efficient solar cells. Using the ferroelectric insulator BaTiO<sub>3</sub> we show how photogeneration and the collection of hot, non-equilibrium electrons through the bulk photovoltaic effect (BPVE) yields a greater-than-unity quantum efficiency. Despite absorbing less than a tenth of the solar spectrum, the power conversion efficiency of the BPVE device under 1 sun illumination exceeds the Shockley–Queisser limit for a material of this bandgap. We present data for devices that feature a single-tip electrode contact and an array with 24 tips (total planar area of 1 × 1 μm<sup>2</sup>) capable of generating a current density of 17 mA cm<sup>-2</sup> under illumination of AM1.5 G. In summary, the BPVE at the nanoscale provides an exciting new route for obtaining high-efficiency photovoltaic solar energy conversion.**

Thermalization of photoexcited carriers with energies in excess of the bandgap limits the power conversion efficiency (PCE)<sup>1</sup>, requiring semiconductor absorbers with longer visible-wavelength bandgaps close to the peak in the solar spectrum where the Shockley–Queisser (S–Q) efficiency is highest and with relatively high carrier lifetime–mobility product. In classic solid-state photovoltaic (PV) devices photogenerated charges are separated by the field developed at a p–n junction, a dye-sensitizer interface<sup>2</sup>, a domain boundary or the field due to the Demer effect. All of these PV effects have an inhomogeneous excitation or spatially inhomogeneous medium and a photovoltage in the unit element that does not exceed the bandgap  $E_g$ . The BPVE<sup>3–5</sup> in non-centrosymmetric crystals is a striking physical phenomenon: the photovoltage generated by the BPVE can greatly exceed  $E_g$ , but the direct conversion of light energy (for example, solar) to electricity is extremely low. Over the past decade, photovoltaic effects in polar materials have attracted renewed attention<sup>6–22</sup>.

Also known as the anomalous photovoltaic effect, the BPVE can be observed in crystals that belong to 20 point groups that lack a centre of inversion symmetry (including ferro- and piezoelectrics). There are two proposed mechanisms of BPVE: ballistic and shift. The ballistic mechanism<sup>5</sup> is associated with the excitation of non-thermalized (hot) carriers in a crystal and is caused by the asymmetric distribution of their momenta. The internal photoeffect is illustrated in Fig. 1 for centrosymmetric and non-centrosymmetric crystals (Fig. 1a,b, respectively). Photoexcited non-thermalized carriers lose their energy and descend to the bottom of the band over free path  $l_0$ . The value of  $l_0$  is material-dependent and is estimated to be on the order of tens to hundreds of nanometres<sup>5,23</sup>. The shift mechanism of the BPVE is quantum-mechanical in nature, obtained by taking into account the non-diagonal elements of the density matrix<sup>10,24</sup>. The BPVE in this case is caused not by the carrier movement in the band, but by the shift  $\bar{R}$  in real space following the carrier band–band transition.

If a homogeneous medium of thickness  $d$  without a centre of symmetry and possessing short-circuited electrodes is subjected to a uniform illumination, it leads to the generation of a steady-state current  $j_{pv}$ , which depends on the intensity and polarization of the light. If the electrodes are disconnected, that is, are in the open-circuit condition,  $j_{pv}$  generates the photovoltage

$$V_{oc} = \frac{j_{pv}d}{\sigma_d + \sigma_{pv}} \quad (1)$$

with the photovoltaic field

$$E_{pv} = j_{pv}/\sigma_{pv} \quad (2)$$

where  $\sigma_d$  and  $\sigma_{pv}$  are the dark- and photoconductivity, respectively, the latter being

$$\sigma_{pv} = eI_0\alpha\phi(\hbar\omega)^{-1}(\mu\tau)_{pv} \quad (3)$$

where  $I_0$  is the light intensity,  $\alpha$  is the absorption coefficient,  $\phi$  is the quantum yield,  $\hbar\omega$  is the incident photon energy and  $\mu$  and  $\tau$  are the mobility and lifetime of the carriers responsible for photoconductivity, respectively. The tensor properties of the linear BPVE current are described by

$$j_{pv}^i = \alpha g_{ijl} e_j e_l I_0 \quad (4)$$

where  $e_j$  and  $e_l$  are the components of the light polarization vector and  $g_{ijl}$  is the corresponding third-rank piezoelectric tensor. For a (001)-oriented BaTiO<sub>3</sub> (BTO) crystal we can assign  $g_{ijk} \equiv g_{31}$ . The corresponding scalar relations are

$$j_{pv} = \alpha g I_0 \quad (5)$$

$$E_{pv} = \frac{g}{\phi(\mu\tau)_{pv}} \frac{\hbar\omega}{e} \quad (6)$$

<sup>1</sup>Department of Materials Science & Engineering, Drexel University, Philadelphia, Pennsylvania 19104, USA. <sup>2</sup>Department of Physics, Drexel University, Philadelphia, Pennsylvania 19104, USA. <sup>3</sup>Department of Electrical & Computer Engineering, Drexel University, Philadelphia, Pennsylvania 19104, USA.

<sup>4</sup>Shubnikov Institute for Crystallography, Russian Academy of Sciences, Leninsky Prospect 59, Moscow, 117333, Russia. <sup>5</sup>Department of Chemistry, University of Pennsylvania, Philadelphia, Pennsylvania 19104, USA. <sup>6</sup>US Naval Research Laboratory, Washington DC 20375, USA. <sup>†</sup>These authors contributed equally to this work. \*e-mail: spanier@drexel.edu

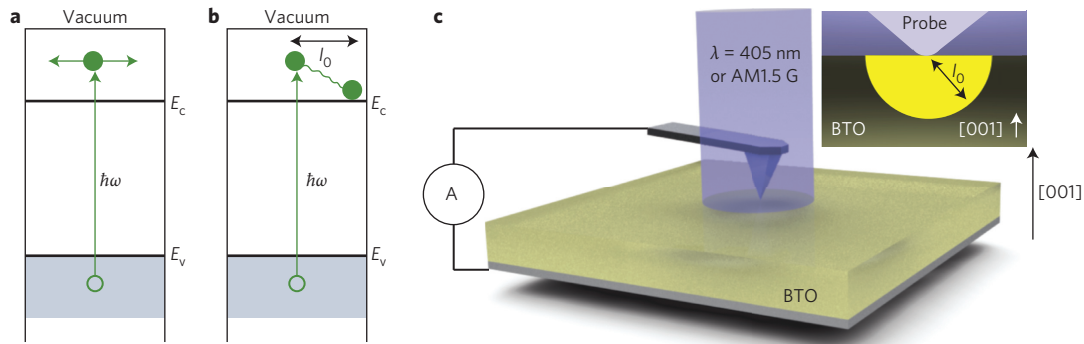


**Figure 1 | Schematic illustrations of the photoexcitation processes. a,** Centrosymmetric crystal. **b,** Non-centrosymmetric crystal. **c,** The experimental configuration, including the thermalization hemisphere of radius  $l_0$  as described in the text.  $E_c$ , conduction band minimum;  $E_v$ , valence band minimum.

For  $\sigma_{pv} \gg \sigma_d$  the photovoltaic field  $E_{pv}$  does not vary with  $I_0$ , but  $j_{pv}$  scales linearly with  $I_0$ .

As it is also the case that

$$j_{pv} = e\alpha I_0 (\hbar\omega)^{-1} \phi \xi^{ex} l_0 \quad (7)$$

where  $\xi^{ex}$  ( $= \xi^{ex}(k_0)$ ) is the photoexcitation asymmetry parameter<sup>5</sup>

$$l_0 = g e^{-1} \hbar\omega (\phi \xi^{ex})^{-1} \quad (8)$$

For a bulk BTO crystal  $g_{31} = 3 \times 10^{-9} \text{ cm V}^{-1}$ ,  $\xi^{ex} = 10^{-3}$  at  $\hbar\omega = 3.06 \text{ eV}$  (ref. 5) and  $l_0 \approx 90 \text{ nm}$ . Because  $\alpha_{BTO} \approx 5\text{--}10 \text{ cm}^{-1}$  at  $\hbar\omega = 3.06 \text{ eV}$  (ref. 25), most of the light is absorbed in the crystal.

The power conversion efficiency  $\eta$ , which can be obtained from equations (1)–(6), is given by  $\eta \approx g E_{pv}$  (ref. 5). For a bulk BTO crystal,  $E_{pv} \approx 100\text{--}200 \text{ V cm}^{-1}$  and  $\eta \approx 10^{-6}\text{--}10^{-7}$ . In equations (3) and (6),  $\mu$  and  $\tau$  are associated with thermalized non-equilibrium carriers, which do not contribute to the BPVE. However, if  $d \approx l_0$ ,  $E_{pv}$  can be increased significantly because all of the photoexcited carriers contribute to the BPVE, significantly raising  $\eta$  (ref. 20). This idea was realized in Pt/BTO/Pt heterostructures with BTO thicknesses of 20 and 40 nm and planar electrodes<sup>20</sup>. The single-wavelength power conversion efficiency of BTO at the nanoscale is  $\eta \approx 10^{-2}$ , an increase of five orders of magnitude in comparison with bulk crystals.

A  $10^7$ -fold enhancement in apparent external quantum efficiency  $\eta_{EQE}$  (to  $\sim 1$ ) in BiFeO<sub>3</sub> using an electrically conductive atomic force microscopy (AFM) probe was reported, but no explanation of its origin or mechanism was provided<sup>8</sup>. It has been assumed that efficient solar PV energy conversion requires a semiconductor with strong optical absorption, carrier separation involving an interface, a reasonable  $\mu\tau$  product and a sizable length over which photoexcited carriers diffuse to reach the contact. Here we demonstrate how, using the BPVE in a nanoscale geometry, extraordinarily high quantum efficiencies and practical power conversion efficiencies can be attained in a polar insulator (BTO). Significantly, we also describe how hot carriers are photogenerated, travel ballistically in a locally intense electric field produced by screening of the spontaneous polarization and are collected from an entire thermalization volume.

We confirmed the ballistic character of the photogenerated BPVE electrons in BTO by measuring the Hall component of the bulk photovoltaic current under illumination at 300 K in a BTO single crystal, obtaining the mobility of the non-thermalized electrons of  $\approx 2,000 \pm 200 \text{ cm}^2 \text{ V}^{-1} \text{ s}^{-1}$  (see Methods). Conductive AFM tips with radii of 25 and 40 nm and a 5  $\mu\text{m}$  radius conductive probe were each placed in contact with the (100) surface of a monodomain BTO crystal that possesses a bottom planar electrode. Samples were

illuminated in three ways: using a  $\lambda = 405 \text{ nm}$  laser (Fig. 1c) with a spot area of  $2 \times 4 \text{ mm}^2$  and spot area-averaged intensities  $I_0$  between 100 and  $470 \text{ mW cm}^{-2}$ , under 1 sun ( $100 \text{ mW cm}^{-2}$ ) AM1.5 G illumination and under a tunable monochromatic light source (see Methods).

Time evolution of the short-circuit current  $I_{sc}$  in BTO using the 25 nm-radius tip is shown in Fig. 2a: screening and pyroelectric current response on illumination is followed by steady state photovoltaic current<sup>26,27</sup>. Using the large-radius (5  $\mu\text{m}$ ) probe and 405-nm illumination, the response in BTO (Fig. 2b, blue) shows a photovoltage  $V_{oc}$  ( $\approx 8 \text{ V}$ ) that far exceeds the bandgap of BTO, with  $I_{sc} \approx 0.2 \text{ nA}$ . In contrast, the response collected from the nearly isostructural, paraelectric perovskite oxide SrTiO<sub>3</sub> ( $E_{g,STO} \approx 3.2 \text{ eV}$ ) exhibits no detectable  $I_{sc}$  or  $V_{oc}$  (Fig. 2b, black). The observed values of  $V_{oc}$  in BTO using the 5  $\mu\text{m}$  and 25 nm radius tips are the same.  $V_{oc}$  is also nearly independent of  $I_0$  (Fig. 2c), in accordance with equation (6).

The electrode area (that is, the contact area of the tip) is normally required for calculating current density and estimating the conversion efficiency. However,  $I_{sc}$  values for the 5  $\mu\text{m}$  and 25 nm radius probe electrodes under comparable illumination intensity are remarkably similar ( $\approx 0.15\text{--}0.2 \text{ nA}$ , Fig. 2b,c), despite the differences in the probe sizes of more than two orders of magnitude. We also find that after lowering the probes enough to observe the onset of a stable current reading,  $I_{sc}$  does not vary with loading and is reproducible after repeatedly raising and lowering the probe, providing further confirmation that the current is independent of the contact area in our experiments. Thus the actual value of  $j_{pv}$  and  $\eta$  cannot be obtained from the actual or effective contact radius of the probe<sup>8</sup>.

Our observed invariance in the measured photocurrent versus the probe size indicates that the response is governed instead by another length scale that is independent of the probe diameter. We propose that the thermalization length  $l_0$  dictates the effective electrode area for current normalization, a hemispherical surface of thermalization over which photogenerated carriers are collected at the probe (that is,  $A \approx 2\pi l_0^2$ ) and we take  $l_0 \approx 100 \text{ nm}$  (ref. 5) as a conservative upper limit for  $\hbar\omega = 3.06 \text{ eV}$ .

The short-circuit current densities for each intensity at  $\hbar\omega = 3.06 \text{ eV}$  are shown in Fig. 3a (left axis), obtained from the  $I_{sc}$  values in Fig. 2b divided by  $A$ . Values of the apparent external quantum efficiency<sup>28</sup>  $\eta_{EQE}$  (Fig. 3a, right axis), expressed as the ratio of the electron flux density through  $A$  to the photon flux density, exceed unity and increase with  $I_0$ . This is due to the increase in the density of non-thermalized electrons due to impact ionization<sup>29</sup>. The BPVE origin of the photoresponse is further confirmed by measuring the variation of the photocurrent with incident photon energy. The photocurrent density  $J_{sc}$  (Fig. 3b) is seen to be non-zero for photon energies well below  $E_g$ , probably due to photoexcitation of oxygen vacancy-bound electrons<sup>25,30</sup>. Measured using a tunable monochromatic source,  $J_{sc}$  varies with photon energy, its

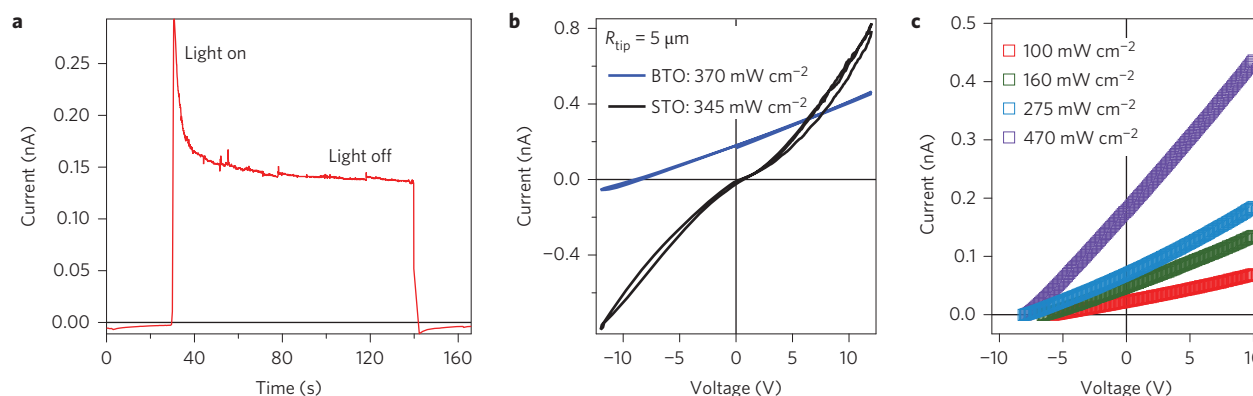


**Figure 2 | Bulk photovoltaic response at the nanoscale in bulk single-domain ferroelectric BTO.** **a**, Time evolution of the short-circuit photocurrent response to monochromatic ( $\lambda = 405$  nm) illumination, showing transient screening and pyroelectric components followed by steady-state photovoltaic components using a 25-nm-radius probe. **b**, Dependence of the photovoltaic current on voltage for the BTO crystal (blue) under the same wavelength of monochromatic illumination compared with that for an STO crystal (black), each using a probe of 5  $\mu\text{m}$  in radius  $R_{\text{tip}}$ . The dark current in BTO was  $<1$  pA (not shown). **c**, Dependence of the photovoltaic current in the BTO crystal on the intensity of the monochromatic illumination intensity using a 25-nm-radius tip.

magnitude peaking near the interband transition and changing sign near 3.8 eV. Its spectral shape is in agreement with previously published experimental and calculated currents for orthogonal optical and ferroelectric polarizations<sup>10,31</sup>. The apparent incident photon-to-collected electron (IPCE) efficiency (Fig. 3c) exceeds unity even for photon energies well below  $E_g$ , providing further evidence of the role of non-thermalized carriers in our BPVE device.

The tip regime of the BPVE in bulk BTO has two key features. First, for excitations within  $l_0$  of the nanoscaled absorber, all of the photogenerated conduction electrons are non-thermalized and

contribute to the BPVE<sup>20</sup>. Second, an intense field is concentrated within the thermalization (and photogenerated collection) length  $l_0$  of the tip electrode, thereby enabling the quantum efficiency to reach and exceed unity. It explains the difference in quantum efficiency between the nanoscaled capacitor<sup>20</sup> and the tip regime. For the tip-electrode geometry, the relationship  $\eta \approx g_{31}E_{\text{pv}}$  (ref. 5) is not valid due to the highly non-uniform field. In monodomain BTO, the very high  $\eta_{\text{EQE}}$  value from excitation by  $\hbar\omega = 3.06 \lesssim E_{g,\text{BTO}}$  arises from several sources: the excitation of oxygen vacancy-bound donor electrons can yield hot carriers with kinetic energies of nearly  $2E_g$  ( $\approx 6.0$  eV) in addition to interband excitation, and the several times higher value of  $g_{31}$  in BTO compared with  $\text{BiFeO}_3$ .

The high value of  $\eta_{\text{EQE}} (>1)$  in the tip geometry has not been explained. It has been proposed<sup>8</sup> that photogenerated carriers may be collected efficiently at some distance away from the contact area of the tip and the scale over which the electric field decays by an order of magnitude was thought to be roughly three times the radius of the tip. We cannot rule out a possible contribution from photoexcited carriers away from the tip, however we propose here two possible mechanisms for high  $\eta_{\text{EQE}}$  values ( $>1$ ) in perovskite ferroelectrics in the tip regime at the surface of ferroelectric oxides. A Debye length  $L_{\text{Debye}}$  is caused by the screening of the spontaneous polarization by the volume charge<sup>32</sup>. In a BTO crystal  $L_{\text{Debye}} \approx 50\text{--}100$  nm. In the tip regime the screening charge is concentrated within a hemisphere of radius  $L_{\text{Debye}}$ , which is comparable to  $l_0$ . It creates high electric field around the tip and can result in impact ionization caused by the non-thermalized high-energy carriers, leading to  $\eta_{\text{EQE}} > 1$ . For planar electrodes the screening field is much lower. Additionally, if the concentration of surface states is not too high ( $<10^{15} \text{ cm}^{-2} \text{ eV}^{-1}$ ) (ref. 33) the screening of spontaneous polarization in a BTO crystal leads to strong band bending near the surface and impact ionization<sup>29</sup>. For example, a photon with energy 3.06 eV excites electron  $e_1$  from an impurity band to the conduction band. The relaxation of  $e_1$  towards the neutral part of the BTO crystal creates a second electron-hole pair  $e_2, h_2$ , by impact-ionized electrons from the impurity band. Thus screening in a ferroelectric semiconductor can lead to multiplication without violating the conservation of either energy or momentum.

A proof of the origin of our mechanism involves similar experiments with GaP under planar and tip electrodes. Although GaP is piezoelectric and exhibits the BPVE, GaP is not ferroelectric—that is, it does not possess spontaneous polarization and therefore does not produce the screening field at the tip. The photocurrent measured on a GaP(100) single crystal exhibits the BPVE, but no enhancement in the photoresponse using the tip is found. This

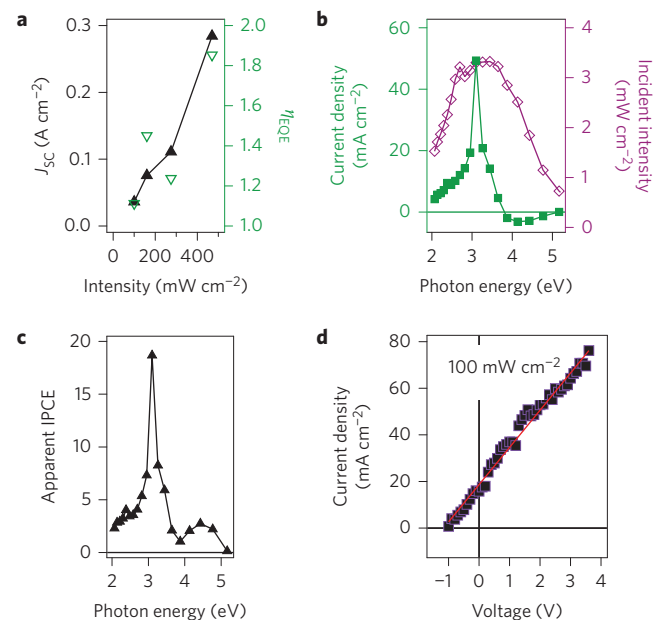


**Figure 3 | Quantum efficiency, photocurrent spectrum and power conversion efficiency in bulk single-domain ferroelectric BTO at the nanoscale.** **a**, Dependence of  $J_{\text{sc}}$  and  $\eta_{\text{EQE}}$  on the incident monochromatic ( $\lambda = 405$  nm) light intensities ranging from 100 to 470  $\text{mW cm}^{-2}$ . **b**, Variation in  $J_{\text{sc}}$  with photon energy (left y axis) and the corresponding incident optical intensity from monochromatically tuned illumination (right y axis). **c**, Apparent IPCE efficiency obtained using the data shown in **b**. **d**, Photovoltaic response under 1 sun AM1.5 G illumination.  $\eta_{\text{EQE}}$ ,  $J_{\text{sc}}$  and IPCE are calculated based on the effective area (surface of thermalization hemisphere) as described in the text.

**Table 1 | Non-thermalized carrier BPVE device characteristics in the BTO(001) crystal.**

Illumination	Intensity (mW cm <sup>-2</sup> )	<i>I</i> <sub>sc</sub> (pA)	<i>J</i> <sub>sc</sub> (mA cm <sup>-2</sup> )	$\eta_{\text{EQE}}$	PCE (%)
405 nm	100	22.8	36.3	1.11	
405 nm	160	47.6	75.8	1.45	
405 nm	275	69.8	111.1	1.24	
405 nm	470	178.7	284.4	1.85	
AM1.5 G	100	12	19.1		4.8

validates that the BPVE and screening in the tip regime enabled by ferroelectricity is the operative mechanism (see Methods and Supplementary Information).

Unlike in conventional devices that are constrained by the S–Q limit, the ability to collect non-thermalized photogenerated carriers should enable a high power conversion efficiency. The *J*–*V* response of this nanoscale tip-electroded monodomain bulk BTO crystal under 1 sun (100 mW cm<sup>-2</sup>) AM1.5 G illumination (see Methods) is shown in Fig. 3d. With  $J_{\text{sc,AM1.5 G}} \approx 19 \text{ mA cm}^{-2}$ ,  $V_{\text{oc}} \approx 1.2 \text{ V}$  and a fill factor of  $\approx 0.21$ , the power conversion efficiency (PCE) is 4.8%, the largest so far reported for any single-layer oxide perovskite or simple ternary (ABO<sub>3</sub>-type) oxide perovskite. Significantly, the PCE for our BTO hot-carrier BPVE device exceeds the S–Q limit for a material with a 3.2 eV bandgap by  $\approx 50\%$ . Table 1 lists the values of  $J_{\text{sc}}$  and  $\eta_{\text{EQE}}$  for monochromatic illumination of different intensities and PCE under 1 sun AM 1.5 G illumination, as indicated.

To provide further experimental verification of the large PCE observed in the single-tip device we produced a hexagonal array of 24 indium tin oxide (ITO) electrodes on the poled, single domain-state, bulk crystal BaTiO<sub>3</sub> (001) spaced equally over a planar area of  $\approx 1 \times 1 \mu\text{m}^2$  (Fig. 4 and Methods). Collection of the photocurrent voltage was carried out by probing the  $1 \mu\text{m}^2$  area device under 1 sun, AM 1.5 G illumination. Here we include the influence of the low-temperature ITO (see Methods) to understand the fraction and frequency distribution of the AM1.5 G light that actually reaches the BaTiO<sub>3</sub> layer. Physical vapour-deposited ITO at low temperatures (<150 °C) produces films with poor optical transmittance in the near ultraviolet<sup>34</sup>. Measurements of the transmissivity for ITO layers deposited with a very similar protocol to ours<sup>34</sup> show a strong reduction in transmissivity with decreasing light wavelength, from 60% at 500 nm to 47% at 450 nm, 20% at 375 nm and 5% at 350 nm. Below 350 nm the transmissivity falls even farther<sup>34</sup>, dropping below 1% at 330 nm. This strongly

frequency-dependent transmissivity means that the light fluence reaching the ITO is strongly attenuated and red-shifted.

Next we use the known wavelength-dependent BaTiO<sub>3</sub> absorption coefficient  $\alpha(\lambda)$  (ref. 25) and the AM1.5 G irradiance profile  $I_0(\lambda)$  of our solar simulator<sup>35</sup> to determine the integrated effect of the ITO transmissivity on the light absorption of BaTiO<sub>3</sub>. Total light absorption can be calculated by integrating the product of absorption coefficient and irradiance  $I(\lambda)$ :

$$A = \int_{\lambda_1}^{\lambda_2} \alpha(\lambda) I(\lambda) d\lambda \quad (9)$$

First we adapt this expression to the experimental conditions. Irradiance is that of the solar simulator  $I_0(\lambda)$ , reduced by the transmissivity of ITO  $T(\lambda)$ :

$$A_{\text{expt}} = \int_{\lambda_1}^{\lambda_2} \alpha(\lambda) I_0(\lambda) T(\lambda) d\lambda \quad (10)$$

We expect that the future deposition of higher-quality transparent electrodes should provide near-unity transmissivity, in an otherwise similar experimental geometry:

$$A_{\text{ideal electrode}} = \int_{\lambda_1}^{\lambda_2} \alpha(\lambda) I_0(\lambda) d\lambda \quad (11)$$

Performing these light absorption calculations numerically for known  $I_0$ ,  $\alpha$ , and  $T$  yields

$$A_{\text{ideal electrode}} / A_{\text{expt}} \approx 30 \quad (12)$$

Thus, the experimental set-up allows 1/30 of the light absorption that full AM1.5 G would provide (Fig. 4b).

On the basis of our experimental set-up, with reduced photocurrent and photovoltage due to ITO attenuating and red-shifting the light reaching the BaTiO<sub>3</sub>, we can deduce the benchmark PCE that would be observed under full AM1.5 G illumination. The quantum efficiency observed for the single tip is above unity (Fig. 3). Therefore, presuming that photocurrent increases linearly with light absorption is a conservative approximation, such that the photocurrent under the full AM1.5 G would be 30 times the experimentally observed photocurrent. Also, the photovoltage is largely independent of incident fluence (Fig. 2c), but it is highly sensitive to the frequency distribution of the light. We assume that the lower photovoltage is due to this redshift, and that a highly transparent electrode would restore the photovoltage to near 1.1 V. Taking into account these considerations, the array of 24 tips with an ideal

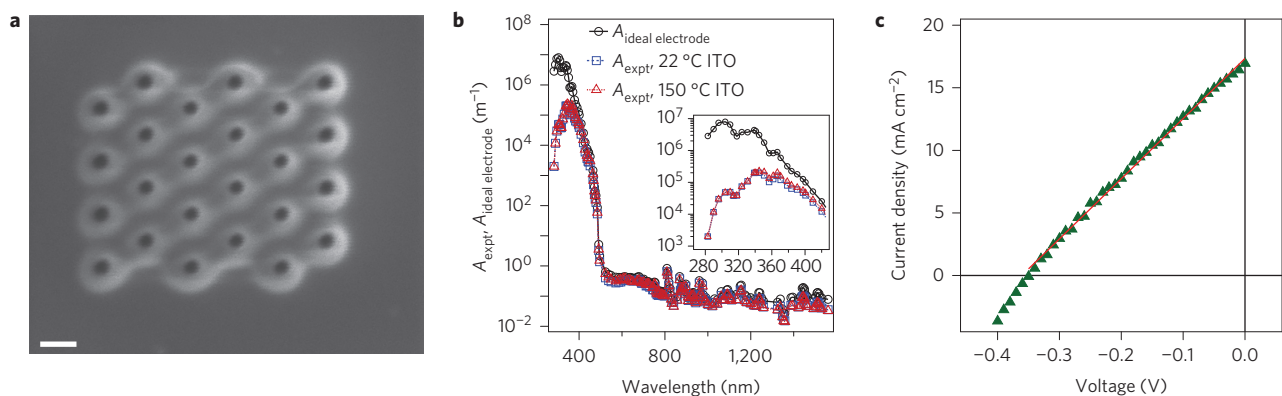


**Figure 4 | Photovoltaic device consisting of an array of nanoscale tips. a**, Plan-view scanning electron micrograph of an array of 24 focused ion beam-milled holes through an SiO<sub>2</sub> layer into a BaTiO<sub>3</sub> (001) crystal before ITO deposition. Scale bar, 200 nm. **b**, The effect of ITO deposited at low temperature on the fraction and frequency distribution of the AM1.5 G light that reaches the BaTiO<sub>3</sub> crystal, showing that our experimental set-up allows 1/30 the light absorption that full AM1.5 G would provide. **c**, The effective current density–voltage response of the 24-electrode array under AM1.5 G (100 mW) as described in the text. The electrode area for the array is the planar area encompassing the nanoscale electrodes ( $1 \mu\text{m}^2$ ).

electrode would yield a photocurrent of 170 pA and a photovoltage of 1.1 V. For the array of  $1 \times 1 \mu\text{m}^2$ , this system will give a photocurrent density of  $17.0 \text{ mA cm}^{-2}$ , yielding a PCE of 3.9% (Fig. 4c).

Thus, under full AM1.5 G illumination, 24 closely spaced tips yield many times the one-tip current. This invalidates the notion that the one-tip result could be explained by collection of carriers over a wide area. If this were true, then the 24 tips would draw from each others' areas, giving no more current than the single tip. The current scaling with the number of tips (maintaining similar current density) confirms that our assumed value for the thermalization length  $l_0$  of 100 nm is reasonable.

High-efficiency conventional solar cells rely on the strong absorption of visible light, the judicious selection of barrier-free electrical contacts, effective separation and the collection of photo-generated carriers within a minimal carrier diffusion length associated with a relatively high carrier lifetime–mobility product and a high ideality factor in pursuit of the S–Q limit. Hot-carrier extraction<sup>36</sup>, multiple exciton generation in semiconductor nanocrystals<sup>37–39</sup> and photon management, that is, solar concentration using an individual nanowire as an optical cavity<sup>28</sup>, have been proposed and pursued as strategies for overcoming the S–Q limit. By contrast, the BPVE at the nanoscale opens new possibilities using hot-carrier management and carrier multiplication. The transport and collection of photogenerated hot non-equilibrium carriers over  $l_0$  in the BPVE is not impeded by the electrode barrier height. Considerable work lies ahead in attaining deeper understanding of the microscopic mechanism(s) and in identifying novel ferroelectric absorbers. Nevertheless the tip electrode-enabled BPVE can now be considered as a promising new paradigm for overcoming conventional power conversion efficiency limits, and optoelectronics in general. With emerging single-phase semiconducting ferroelectrics exhibiting solar spectrum-relevant absorption<sup>15,19</sup>, the nanoscale BPVE may provide a fundamentally new route for third-generation<sup>40,41</sup> photovoltaic solar energy conversion.

## Methods

Methods and any associated references are available in the [online version of the paper](#).

Received 20 October 2015; accepted 23 June 2016;  
published online 8 August 2016; corrected after print 31 August 2016

## References

- Shockley, W. & Queisser, H. J. Detailed balance limit of efficiency of p–n junction solar cells. *J. Appl. Phys.* **32**, 510–519 (1961).
- O'Regan, B. & Gratzel, M. A low-cost, high-efficiency solar cell based on dye-sensitized TiO<sub>2</sub> films. *Nature* **335**, 737–740 (1991).
- Grekov, A. A., Malitskaya, M. A., Spitsina, V. D. & Fridkin, V. M. Photoelectric effects in A<sup>3</sup>B<sup>6</sup>C<sup>7</sup>-type ferroelectrics-semiconductors with low-temperature phase transitions. *Kristallografiya* **15**, 500–509 (1970).
- Glass, A. M., von der Linde, D. & Negran, T. J. High-voltage bulk photovoltaic effect and the photorefractive process in LiNbO<sub>3</sub>. *Appl. Phys. Lett.* **25**, 233–235 (1974).
- Sturman, B. & Fridkin, V. *The Photovoltaic and Photorefractive Effects in Noncentrosymmetric Materials* (Gordon and Breach, 1992).
- Yang, S. Y. *et al.* Above-bandgap voltages from ferroelectric photovoltaic devices. *Nature Nanotech.* **5**, 143–147 (2010).
- Seidel, J. *et al.* Efficient photovoltaic current generation at ferroelectric domain walls. *Phys. Rev. Lett.* **107**, 126805 (2011).
- Alexe, M. & Hesse, D. Tip-enhanced photovoltaic effects in bismuth ferrite. *Nature Commun.* **2**, 256 (2011).
- Nechache, R. *et al.* Photovoltaic properties of Bi<sub>2</sub>FeCrO<sub>6</sub> epitaxial thin films. *Appl. Phys. Lett.* **98**, 202902 (2011).
- Young, S. M. & Rappe, A. M. First principles calculation of the shift current photovoltaic effect in ferroelectrics. *Phys. Rev. Lett.* **109**, 116601 (2012).
- Young, S. M., Zheng, F. & Rappe, A. M., First-principles calculation of the bulk photovoltaic effect in bismuth ferrite. *Phys. Rev. Lett.* **109**, 236601 (2012).
- Kreisel, J., Alexe, M. & Thomas, P. A. A photoferroelectric material is more than the sum of its parts. *Nature Mater.* **11**, 260 (2012).
- Daranciang, D. *et al.* Ultrafast photovoltaic response in ferroelectric nanolayers. *Phys. Rev. Lett.* **108**, 087601 (2012).
- Yang, B. *et al.* Tuning the energy level offset between donor and acceptor with ferroelectric dipole layers for increased efficiency in bilayer organic photovoltaic cells. *Adv. Mater.* **24**, 1455–1460 (2012).
- Grinberg, I. *et al.* Perovskite oxides for visible-light-absorbing ferroelectric and photovoltaic materials. *Nature* **503**, 509–512 (2013).
- Fridkin, V. Parity nonconservation and bulk photovoltaic effect in a crystal without symmetry center. *IEEE Trans. Ultrason. Ferroelect. Freq. Control* **60**, 1551–1555 (2013).
- Bhatnagar, A., Roy Chaudhuri, A., Heon Kim, Y., Hesse, D. & Alexe, M. Role of domain walls in the abnormal photovoltaic effect in BiFeO<sub>3</sub>. *Nature Commun.* **4**, 2835 (2013).
- Xiao, Z. *et al.* Ferroelectric materials: synthesis and application of ferroelectric P(VDF-TrFE) nanoparticles in organic photovoltaic devices for high efficiency. *Adv. Energy Mater.* **3**, 1581–1588 (2013).
- Nechache, R. *et al.* Bandgap tuning of multiferroic oxide solar cells. *Nature Photon.* **9**, 61–67 (2015).
- Zenkovich, A. *et al.* Giant bulk photovoltaic effect in thin ferroelectric BaTiO<sub>3</sub> films. *Phys. Rev. B* **90**, 161409 (2014).
- Yuan, Y., Xiao, Z., Yang, B. & Huang, J. Arising applications of ferroelectric materials in photovoltaic devices. *J. Mater. Chem. A* **2**, 6027–6041 (2014).
- Chakrabarty, J. P., Nechache, R., Harnagea, C. & Rosei, F. Photovoltaic effect in multiphase Bi-Mn-O thin films. *Opt. Express* **22**, A80–A89 (2014).
- Malinovskii, V. K. & Sturman, B. I. Photoelectric effects in ferroelectrics with high-mobile nonequilibrium electrons. *Ferroelectrics* **43**, 125–129 (1982).
- von Baltz, R. & Kraut, W. Theory of the bulk photovoltaic effect in pure crystals. *Phys. Rev. B* **23**, 5590–5596 (1981).
- Wemple, S. H., DiDomenico, M. & Camlibel, I. Dielectric and optical properties of melt-grown BaTiO<sub>3</sub>. *J. Phys. Chem. Solids* **29**, 1797–1803 (1968).
- Chynoweth, A. G. Surface space-charge layers in barium titanate. *Phys. Rev.* **102**, 705–714 (1956).
- Chen, F. S. Optically induced change of refractive indices in LiNbO<sub>3</sub> and LiTaO<sub>3</sub>. *J. Appl. Phys.* **40**, 3389–3396 (1969).
- Krogstrup, P. *et al.* Single-nanowire solar cells beyond the Shockley-Queisser limit. *Nature Photon.* **7**, 306–310 (2013).
- Kolodinski, S., Werner, J. H., Wittchen, T. & Queisser, H. J. Quantum efficiencies exceeding unity due to impact ionization in silicon solar cells. *Appl. Phys. Lett.* **63**, 2405–2407 (1993).
- Berglund, C. N. & Braun, H. J. Optical absorption in single-domain ferroelectric barium titanate. *Phys. Rev.* **164**, 790–799 (1967).
- Koch, W. T. H., Munser, R., Ruppel, W. & Wurfel, P. Anomalous photovoltage in BaTiO<sub>3</sub>. *Ferroelectrics* **13**, 305–307 (1976).
- Jona, F. & Shirane, G. *Ferroelectric Crystals* (Dover, 1962).
- Fridkin, V. *Ferroelectric Semiconductors* (Consultants Bureau, 1980).
- Kang, M., Kim, I., Chu, M., Kim, S. W. & Ryu, J.-W. Optical properties of sputtered indium-tin-oxide thin films. *J. Kor. Phys. Soc.* **59**, 3280–3283 (2011).
- Data for Newport model LCS-100 94011A AM1.5G Fig. 1*; <https://assets.newport.com/webDocuments-EN/images/32057.pdf>
- Ross, R. & Nozik, A. Efficiency of hot-carrier solar energy converters. *J. Appl. Phys.* **53**, 3813–3818 (1982).
- Schaller, R. D. & Klimov, V. I. High efficiency carrier multiplication in PbSe nanocrystals: implications for solar energy conversion. *Phys. Rev. Lett.* **92**, 186601 (2004).
- Nozik, A. J. *et al.* Semiconductor quantum dots and quantum dot arrays and applications of multiple exciton generation to third-generation photovoltaic solar cells. *Chem. Rev.* **110**, 6873–6890 (2010).
- Semonin, O. E. *et al.* Peak external photocurrent quantum efficiency exceeding 100% via MEG in a quantum dot solar cell. *Science* **334**, 1530–1533 (2011).
- Green, M. *Third Generation Photovoltaics: Ultra-High Efficiency at Low Cost* (Springer, 2006).
- Conibeer, G. Third-generation photovoltaics. *Mater. Today* **11**, 42–50 (2007).

## Acknowledgements

The authors thank L. Tan, F. Zheng, E. J. Mele, J. B. Baxter and I. Grinberg for discussions. J.E.S. acknowledges the support of the US Army Research Office through grant no. W911NF-14-1-0500. A.M.R. acknowledges the support of the Department of Energy through grant no. DE-FG02-07ER46431. Y.Q. and C.J.H. acknowledge the support of the Office of Naval Research through grant no. N00014-14-1-0761. S.M.Y. was supported by a National Research Council Research Associateship Award at the US Naval Research Laboratory. The authors acknowledge core materials characterization facilities at Drexel for access to electron and focused ion beam microscopy, including instrumentation supported by the National Science Foundation under grant no. DMR 0722845. The authors also acknowledge additional support from the National Science Foundation and the Semiconductor Research Corporation under the Nanoelectronics in 2020 and Beyond Program under grant no. DMR 1124696.

**Author contributions**

V.M.F. and J.E.S. proposed the ideas and designed the experiments. V.M.F., A.R.A., Z.G., C.J.H., D.I., A.L.B.-J. and G.X. designed the optical and optoelectronic set-ups, collected photogenerated Hall and photocurrent data, and performed optical and microscopy measurements. J.E.S., V.M.F., A.M.R., A.P., S.M.Y., Y.Q. and C.L.J. contributed to analyses of the data and results, and validation of the model, including simulations. J.E.S. and V.M.F. wrote the manuscript, and with A.M.R., A.P., S.M.Y. and Y.Q., edited the manuscript.

**Additional information**

Supplementary information is available in the [online version of the paper](#). Reprints and permissions information is available online at [www.nature.com/reprints](http://www.nature.com/reprints). Correspondence and requests for materials should be addressed to J.E.S.

**Competing financial interests**

The authors declare no competing financial interests.

## Methods

**Materials, probes, ferroelectric poling and illumination and geometry.** BaTiO<sub>3</sub> (001), SrTiO<sub>3</sub> (100) and GaP(100) crystals (MTI, CA) of 1.0, 0.5 and 0.5 mm in thickness, respectively, and each 5 × 5 mm<sup>2</sup> in area were used. Silver paste was introduced to one face of each crystal as the bottom contact, and the BaTiO<sub>3</sub> crystal was poled along [001] at 300 K at >750 V for 100 s following the collection of ferroelectric hysteresis loops in an atmosphere (Precision LC ferroelectric tester interfaced with a high-voltage source and amplifier, Radiant Technologies, Inc., New Mexico). Following poling of the BaTiO<sub>3</sub> crystal, both crystals were placed in an optically accessible vacuum probe station (Lakeshore TTP4). Electrical contact with the top of each crystal was attained by using probes of several different radii, specifically 5 μm tungsten-coated probes, an AFM probe (Nanoworld Pointprobe, <25 nm radius, including an electrically conductive layer of PtIr<sub>3</sub>) or ≈40 nm radius Pt-coated tips (MikroMasch DPE-XSC11) mounted onto the end of the tungsten probe using Ag paste. Current–voltage data were collected under dark conditions and under monochromatic (λ = 405 nm) illumination over an elliptical area of ~8 mm<sup>2</sup> with selected intensities ranging from 100–470 mW cm<sup>-2</sup>, under tunable monochromatic illumination (Horiba PowerArc 75W Xe lamp and 0.2 m f/4 monochromator) from 200 nm < λ < 600 nm producing a 20 nm spectral bandwidth, with light routed to the sample through a quartz fibre and optical collimator producing a spot of 6.4 mm in diameter with intensities ranging from 0.8–3.3 mW cm<sup>-2</sup>. The samples were illuminated from the top of the tip, and within ≈5° of the normal to the sample plane. In all cases, the incident optical polarization was lying in the (001) plane, perpendicular to the direction of ferroelectric polarization. Data were collected for the 40 nm radius probe using a λ = 405 nm laser, producing an elliptical spot area of ≈8 mm<sup>2</sup> and spot area-averaged intensity of 675 mW cm<sup>-2</sup>. Measured photocurrents were normalized to reference intensities at each wavelength using a calibrated optical power meter (Gentec Maestro). The monodomain state was verified systematically following poling under this field using crossed linear optical polarizers and after measurements, confirming that our experiments were conducted in the monodomain state at all times. Current–voltage data were also collected under 1 sun AM1.5 G illumination (100 mW cm<sup>-2</sup>, Newport LCS-100) where a reference cell-calibrated ORIEL/Newport model LCS-100 94011A class A AM1.5 G solar simulator was used following certification under IEC 60904-9 Ed.2, ASTM E927-05 and JIS C8912 standards, including spectral match. A 1 inch × 1 inch mask/aperture was used for measurements, and no change in the short-circuit current density was observed with the removal of the mask.

**Experimental procedures.** Data were conducted both under vacuum (10<sup>-6</sup> torr) and under an atmosphere, all at 300 K. Positive voltage refers to the positive voltage applied to the tip with respect to the bottom electrode. A positive bias was applied to the tip of the top contact while it was held above the surface and not in contact. The current was then monitored while the tip was lowered slowly until a steady current was observed. Current–voltage sweeps were collected (Keithley SCS-4200) starting from zero bias, proceeding to positive bias to the maximum voltage of +10 V, returning to zero and proceeding without interruption to negative bias voltage, then returning to zero. The voltage sweep rate was ≈0.2 V s<sup>-1</sup>, and dwell times per point ranged from 0.12 to 1 s. Several traces were collected successively in the same location as well as in different locations on the crystal using multiple tips of the same and different types. Forces ranging from 5–500 nN were applied during contact of the AFM tip producing no discernible change in short-circuit current with change in loading. Several AFM tips were imaged using high-resolution scanning electron microscopy (Zeiss VP50) to confirm that the tip radius did not become fractured or significantly blunted after probing. Eighteen probing locations were tested using one substrate and nine using another substrate. Observed variations in the short-circuit

current and photovoltage did not exceed ≈15%. PV responses under monochromatic (405 nm) illumination were collected on the same day as sample poling and on the 2nd and 19th days after sample poling. Comparing the set of initial responses with those obtained after 19 days of shelf-life stored in a desiccator under room lighting, the differences between the average values of short-circuit current and photovoltage were found to be ≈5.4% and ≈2.9%, respectively. The PV response was measured 45 days later after storing the sample at room temperature in ambient, and the measured photovoltage and photocurrent values were found to be consistent with the initial results. Under continuous monochromatic (405 nm) irradiation, short-circuit currents reached steady-state values after several tens of seconds or less in all cases, after which variations were observed to be within 1% of the mean. No decrease was observed over 10 min. of testing under continuous illumination.

**Quantum efficiency.** An apparent  $\eta_{EQE}$  is the magnitude of  $J_{sc}e^{-1}$  (in electrons per second per area) divided by the number of photons incident per second per area, that is  $I_0 (1.6 \times 10^{-19}/h\omega)$  (in photons per second per area)<sup>8,28</sup>. An apparent IPCE is presented as the value of  $\eta_{EQE}$  for each photon energy measured. For the calculation of PCE, the fill factor was obtained in the usual manner, by dividing the power at its peak magnitude  $P_{max}(=d(IV)/dV)$  by that for the theoretical maximum for the cell, that is, the power that is the product of  $V_{oc}$  and  $I_{sc}$ .

**Photo-Hall measurement.** The Hall component of the bulk photovoltaic current was measured along [100] at 300 K in a monodomain BaTiO<sub>3</sub> (001) single crystal (5 × 5 mm<sup>2</sup>, 2 mm in thickness) under steady-state unpolarized optical illumination (405–500 nm, 500 mW, in the [001] direction incident over an area of ≈3 × 3 mm<sup>2</sup>, from a bandpass-filtered Hg vapour lamp) through a semitransparent Al contact evaporated on the (001) surface. A magnetic field (2 T) was applied along [010]. The experimental geometry is presented in the Supplementary Information.

**Preparation of the nanoscale tip array device.** The hexagonal array of tips was produced using a series of steps. First, a 50 nm-thick layer of SiO<sub>2</sub> was sputtered onto the entire (001) surface of the crystal. A thin carbon coating was deposited to mitigate electron- and ion-beam charging effects, and focused ion beam milling (FEI Strata DB235) was used to prepare an array of 24 hexagonally arranged column-like holes through the SiO<sub>2</sub>, extending ≈10 nm into the BaTiO<sub>3</sub> crystal. The focused ion beam process followed a series of test milling runs to optimize the accelerating voltage, beam current and exposure time to produce discrete holes of sufficient depth and lateral fidelity. Following this, the carbon coating was removed and SEM and topographic height AFM were carried out to verify that the milling process resulted in holes that extend into the BaTiO<sub>3</sub> surface. Next, an ITO coating was deposited through a shadow mask via pulsed laser deposition at <100 °C under 30 × 10<sup>-3</sup> torr and 1.1 sccm of O<sub>2</sub>, filling the holes with ITO and adding a planar layer. This results in a large ≈85 × 85 μm<sup>2</sup> electrode on top of the SiO<sub>2</sub> layer that connects to the 24 nanoscale electrodes. For current to flow it must cross from the BaTiO<sub>3</sub> to the ITO nanoscale electrodes to the large top ITO electrode. ITO deposition was carried out well below the ferroelectric phase transition temperature  $T_c$  to avoid thermal overshoot and de-poling and/or destruction of the single ferroelectric domain state of the BaTiO<sub>3</sub> crystal. This low-temperature growth produced material with low transparency, as discussed in the main text. The holes are tapered near the bottom: each ITO electrode radius in the SiO<sub>2</sub> layer is ≈50 nm, and the radius at the base of the electrode where it connects to the BaTiO<sub>3</sub> is estimated to be ≈25 nm, based on the milling profile. The electrode spacings (edge to edge) at the surface are estimated to be ≈200 nm at the surface and ≈250 nm at the base of the electrode.

## Erratum: Power conversion efficiency exceeding the Shockley–Queisser limit in a ferroelectric insulator

Jonathan E. Spanier, Vladimir M. Fridkin, Andrew M. Rappe, Andrew R. Akbashev, Alessia Polemi, Yubo Qi, Zongquan Gu, Steve M. Young, Christopher J. Hawley, Dominic Imbrenda, Geoffrey Xiao, Andrew L. Bennett-Jackson and Craig L. Johnson

*Nature Photonics* **10**, 611–616 (2016); published online 8 August 2016; corrected after print 31 August 2016.

In the version of this Article originally published, in Fig. 3a, the units on the left-hand  $y$  axis were incorrect; they should have read '(A cm<sup>-2</sup>)'. This has now been corrected in the online versions of the Article.